Measuring overcast colors with all-sky imaging

Raymond L. Lee, Jr.
Mathematics & Science Division, United States Naval Academy, Annapolis, Maryland 21402, USA
*raylee@usna.edu

Received 18 April 2008; accepted 5 June 2008;
posted 30 June 2008 (Doc. ID 92909); published 12 September 2008

Digital images of overcast skies as seen from the earth's surface open new windows onto the angular details of overcast colors and visible-wavelength spectra. After calibration with a spectroradiometer, a commercial CCD camera equipped with a fisheye lens can produce colorimetrically accurate all-sky maps of overcast spectra. Histograms and azimuthally averaged curves of the resulting chromaticities show consistent, but unexpected, patterns in time-averaged overcast colors. Although widely used models such as LOWTRAN7 and MODTRAN4 cannot explain these characteristic patterns, a simple semiempirical model based on the radiative transfer equation does, and it provides insights into the visible consequences of absorption and scattering both within and beneath overcasts. © 2008 Optical Society of America

OCIS codes: 010.1290, 010.1615, 010.1690, 010.7295, 290.1090, 330.1730.

1. Introduction

Although the words "overcast" and "color" seem unlikely companions, daytime cloudy skies exhibit colors ranging from the apparent monochromes of stratus layers to the remarkable variegation of stratocumulus (Sc) overcasts. Minnaert conducted some of the earliest research on cloud colors, and despite the little known quantitatively about them in his day [1], he nonetheless offered several useful qualitative insights. Among these was that the colors of distant cumuli are affected by the changing balance between (1) bluish airlight scattered toward an observer and (2) yellowish extinction of scattered cloud light over long optical paths. Middleton extended these ideas in his colorimetric modeling of the colors of distant objects seen through clear or hazy atmospheres [2], although he did not analyze similar colors seen beneath overcasts. This early work has hardly been followed by a flurry of activity: papers that measure and model overcast chromaticities or visible-wavelength spectra are rare indeed [3–6], and those that examine the *angular* distribution of overcast colors seem nonexistent. However, recent advances in digital image analysis now let us measure the angular color variations that Minnaert could only outline.

2. Spectral and Colorimetric Calibration of Skylight Cameras

For several decades, researchers in numerous fields have devised techniques for recovering quantitatively accurate color and spectral information from digitized photographs [7–9]. The central problem faced by all such techniques is calibrating the digital imaging system's response to a wide range of scene spectral radiances L_λ at visible wavelengths λ. In trichromatic systems such as red–green–blue (RGB) digital still cameras, the recovered spectra are only metamers for the original scene's L_λ. This is true because each sensor pixel's RGB data provide only three broadband measures of the spectral power distribution, rather than the much larger number of L_λ that typically specify the original (say, 30–100 L_λ for a 400–700 nm visible spectrum). Strictly speaking, then, all such recovered spectra are underdetermined.

Yet Nieves *et al.* have shown recently that if a calibrated camera photographs only scenes whose L_λ are similar to those in the calibration training set, then the recovered spectra are quite realistic both colorimetrically and spectrally [10]. Their simple, yet computationally robust, calibration algorithm permits accurate reconstructions of spectra for various

---

0003-6935/08/34H106-10$15.00/0

Report Documentation Page

Form Approved
OMB No. 0704-0188

1. REPORT DATE **APR 2008**	2. REPORT TYPE	3. DATES COVERED **00-00-2008 to 00-00-2008**

4. TITLE AND SUBTITLE **Measuring overcast colors with all-sky imaging**	5a. CONTRACT NUMBER 5b. GRANT NUMBER 5c. PROGRAM ELEMENT NUMBER
6. AUTHOR(S)	5d. PROJECT NUMBER 5e. TASK NUMBER 5f. WORK UNIT NUMBER
7. PERFORMING ORGANIZATION NAME(S) AND ADDRESS(ES) **United States Naval Academy (USNA),Mathematics & Science Department,Annapolis,MD,21402**	8. PERFORMING ORGANIZATION REPORT NUMBER
9. SPONSORING/MONITORING AGENCY NAME(S) AND ADDRESS(ES)	10. SPONSOR/MONITOR’S ACRONYM(S) 11. SPONSOR/MONITOR’S REPORT NUMBER(S)

12. DISTRIBUTION/AVAILABILITY STATEMENT
Approved for public release; distribution unlimited

13. SUPPLEMENTARY NOTES

14. ABSTRACT

15. SUBJECT TERMS

16. SECURITY CLASSIFICATION OF:			17. LIMITATION OF ABSTRACT	18. NUMBER OF PAGES	19a. NAME OF RESPONSIBLE PERSON
a. REPORT **unclassified**	b. ABSTRACT **unclassified**	c. THIS PAGE **unclassified**	**Same as Report (SAR)**	**10**	

Standard Form 298 (Rev. 8-98)
Prescribed by ANSI Std Z39-18

families of light sources (e.g., daylight at high unrefracted sun elevations h_0 or skylight at low h_0). The spectral family studied here is overcasts with $h_0 \geq 10°$, since radiometer spectra acquired during our earlier work [6] indicate that overcast color changes appreciably at lower h_0. My chief modification to the Nieves calibration procedure is to build the L_λ training set from directly measured rather than diffusely reflected skylight spectra.

To do so, I use a Photo Research PR-650 spectroradiometer that has a spectral range of 380–780 nm, a step size of 4 nm [11], and a telescopic lens that permits radiance measurements across a 1° diameter field of view (FOV). As shown in Fig. 1, a metal bracket is mounted on a tripod so that the aims of the attached cameras and radiometer remain fixed with respect to one another. After sighting through the radiometer's telescope on a distant target and then photographing it, I can match the radiometer's circular FOV with the corresponding 1° diameter circle on each camera's sensor array. Then the radiometer's L_λ are those that generate the camera's RGB values averaged across the 1° circular FOV. All photographs are taken with each camera recording in its 12 bit/channel RAW mode (which has a fixed spectral response), and the only image processing done is to multiply all RGB values by a constant linear gain factor. This fixed stretching of image histograms makes photographs legibly bright but in no way changes the camera spectral response.

Because many daylight and skylight spectra are fairly simple variants on extraterrestrial sunlight, studies consistently show that the first few eigenvectors (typically 3–5) of a principal-components analysis can reproduce these spectra with great accuracy [5,12,13]. The calibration algorithm that Nieves *et al.* call their "direct pseudo-inverse transform" [10] exploits this reduced dimensionality of daylight and skylight spectra, with the added advantages that one need not (1) calculate eigenvectors for the training set of spectra or (2) determine spectral sensitivities for a camera's color channels.

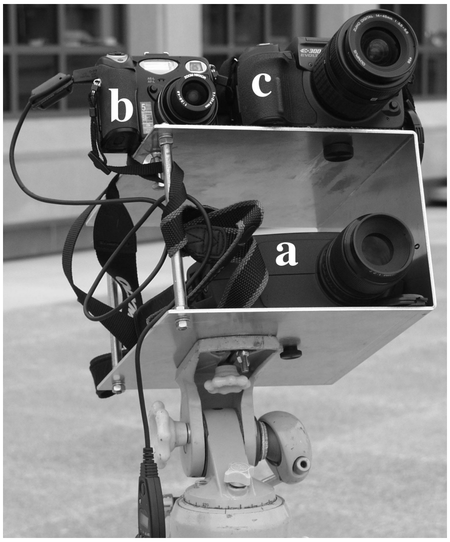

Fig. 1. Spectral and colorimetric calibration equipment consists of two digital still cameras (a Nikon E5000 and an Olympus E300, labeled "b" and "c," respectively) and a Photo Research PR-650 spectroradiometer (labeled "a") affixed to a metal bracket, which is itself mounted on a tripod.

Separate tests with a monochromator and a narrow bandpass filter show that the digital cameras I use (see Fig. 1) respond to L_λ throughout the visible, here taken to be 400–700 nm. At the radiometer's 4 nm resolution, this gives 76 L_λ per visible spectrum. To reconstruct such spectra, I start by using a camera's three unfiltered RGB channels to form the 76 × 3 transform matrix **F** defined by

$$\mathbf{F} = \mathbf{L}\boldsymbol{\rho}^{\mathbf{T}}(\boldsymbol{\rho}\boldsymbol{\rho}^{\mathbf{T}})^{-1}, \tag{1}$$

where **L** is a $76 \times n$ matrix of n different skylight radiance spectra measured with the radiometer (the training set of spectra), $\boldsymbol{\rho}$ is the corresponding $3 \times n$ matrix of normalized 12 bit/channel RGB pixel values for the same n features, and $\boldsymbol{\rho}^{\mathbf{T}}$ is $\boldsymbol{\rho}$'s transpose. My current training set uses measurements from five different overcasts, and it has $n = 232$ features of widely varying color and brightness. To use the resulting least-squares transform matrix **F**, I photograph a new overcast feature with the camera still operating in its native RAW mode. This new feature's reconstructed 76 × 1 spectrum $\mathbf{L_r}$ is then given by

$$\mathbf{L_r} = \mathbf{F}\boldsymbol{\rho}_{\mathbf{r}}, \tag{2}$$

where $\boldsymbol{\rho}_{\mathbf{r}}$ is the feature's 3 × 1 matrix of RGB pixel values. Because **F** is derived from similar spectra, the resulting spectral errors in $\mathbf{L_r}$ will be small. Errors in CIE 1976 u', v' chromaticities calculated from $\mathbf{L_r}$ can be reduced ~12%–21% by applying nonlinear spectral corrections to $\mathbf{L_r}$. These spectral multipliers are calculated by (1) forming n different spectra of the wavelength-by-wavelength ratios of $\mathbf{L} : \mathbf{L_r}$ in the training set and (2) weighting each of these n correction spectra by its inverse colorimetric distance from the new feature's $\mathbf{L_r}$.

The high quality of the reconstructed $\mathbf{L_r}$ is evident in Fig. 2, which shows the 95th percentile root-mean-square error (RMSE) between the radiometer and Nikon E5000 camera spectra for a set of measurements *not* included in the calibration training set. In other words, only 5% of all $\mathbf{L_r}$ reconstructed from Nikon camera data can be expected to generate a RMSE larger than Fig. 2's small 0.22% difference. Reconstructed chromaticities are equally accurate: when compared with radiometer spectra not in the training set, the corresponding Nikon $\mathbf{L_r}$ yield a mean colorimetric error of $\Delta u'v' = 0.000359$ and a $\Delta u'v'$ standard deviation of 0.000230 [14]. This error is clearly subthreshold because it is <30% of the mean MacAdam just-noticeable difference (or JND) [15] for all overcast chromaticities measured with the radiometer.

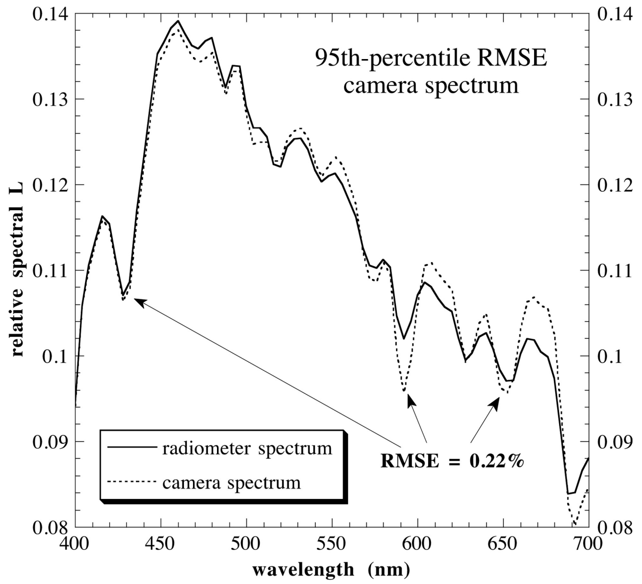

Fig. 2. Normalized radiances for the 95th percentile RMSE spectrum reconstructed from Nikon E5000 camera data compared with the original radiometer spectrum of an overcast feature. Each curve is normalized so that its spectral radiances L_λ satisfy $\sum(L_\lambda)^2 = 1$.

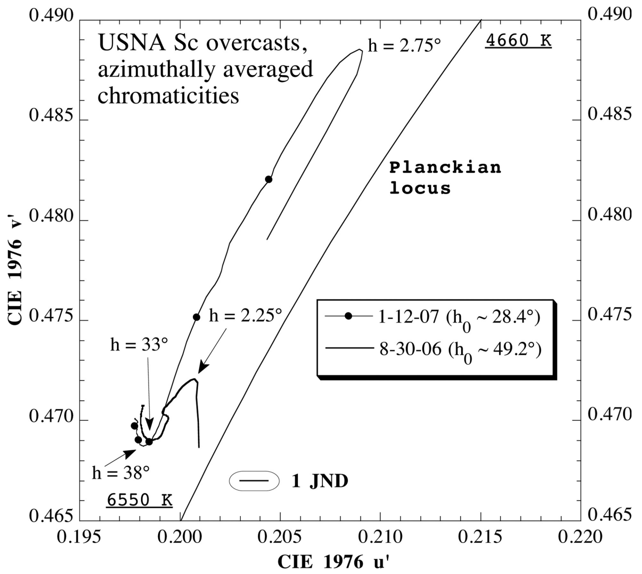

Fig. 3. Portion of the CIE 1976 UCS diagram, showing Sc overcast chromaticities u', v' measured at USNA in Annapolis, Maryland, on 30 August 2006 and 12 January 2007. Each curve plots temporally and azimuthally averaged chromaticities versus view-elevation angle h above the astronomical horizon; the mean unrefracted sun elevation h_0 during each curve's photography session (here, ~38 min) is also listed.

3. Colorimetry of Overcasts from All-Sky Photographs

Overcast skies yield an embarrassment of remote-sensing riches: cloud optical depths τ, radiances, and colors all can vary greatly over distances of a few degrees and time intervals of a few seconds. One especially useful tool for capturing meaningful details from this endlessly mutable scene is a combination of fisheye lens and camera that records a 180° FOV. After equipping Fig. 1's Nikon E5000 with a FC-E8 fisheye converter lens [16], my midshipman research students and I at the U. S. Naval Academy (USNA) in Annapolis, Maryland, took more than 1300 such fisheye photographs of 20 different overcasts from August 2006 through February 2008.

As in our earlier work [6,17], overcasts are defined here as having cloud cover sufficient to obscure any visible clear sky and to make any cast shadows indistinct. Although most of the USNA overcast images were of nonprecipitating Sc, stratus, and altostratus, with careful lens cleaning it was also possible to photograph overcasts during drizzle, light rain, and snow. The resulting all-sky data on overcast spectra and colors offer several surprises.

A. Azimuthally Averaged Chromaticity Curves

For example, Fig. 3 shows a closeup view of the CIE 1976 UCS diagram, including such colorimetric landmarks as part of the Planckian locus and its corresponding color-temperature limits. The short horizontal line labeled "1 JND" is a perceptual ruler whose length is that of a representative MacAdam JND for Fig. 3's two Sc overcasts at USNA. Each curve extends from the zenith (view-elevation angle $h = 90°$) to near the horizon ($h = 0°$), and each plots reconstructed chromaticities averaged over sky azimuths (i.e., along almucantars). Because overcast radiances are often taken to be uniform along almucantars [18], this choice of averaging direction is reasonable if not unassailable [19].

To reduce radiance and color fluctuations at each pixel caused by short-term changes in cloud τ [17], photographs were taken at 30 s intervals and averaged over ~38 min in Fig. 3 to form a mean image of each overcast (see Fig. 4). In my experience, such time periods are long enough to produce useful colorimetric smoothing yet brief enough to capture many important short-term overcast features. Two potentially misleading details are noteworthy in Fig. 4. First, averaging makes these mean Sc images resemble stratus. Second, the faint arcs that stretch from horizon to horizon in Fig. 4(b) are not crepuscular rays but instead are caused by persistent maxima in cloud τ along the mean flow, and these arcs are sometimes accompanied by gravity waves nearly perpendicular to them.

Each Fig. 3 chromaticity curve derived from Fig. 4 has a pair of extrema, with one such colorimetric turning occurring at $h \sim 33°$ or $h \sim 38°$ and the other at $h \sim 2.25°$ or $h \sim 2.75°$, respectively. While these h values vary widely across overcasts, the turnings themselves are quite common features: as we look from high to low h, the first turning is counterclockwise, and the second is clockwise. For the 12 January 2007 overcast, Fig. 3 restricts azimuthal averages to a 167° wide sector that includes a bright yellowish overcast area near the horizon (see the 10 o'clock position in Fig. 4(b)), and this area accounts for Fig. 3's comparatively large color gamut at low h. Obviously this brightening is caused by reduced cloud τ or even

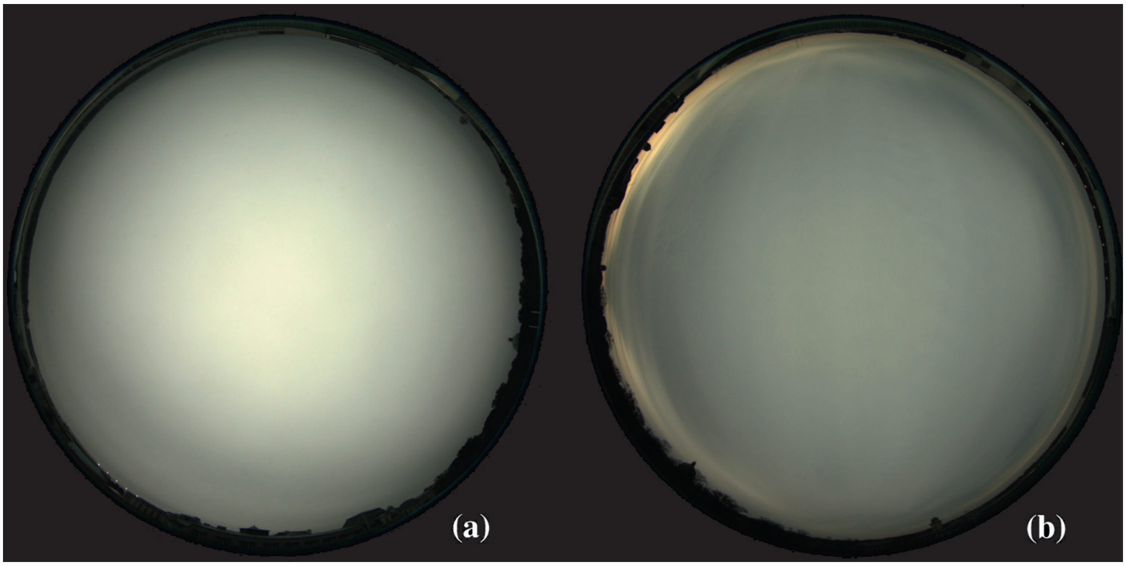

Fig. 4. Time-averaged fisheye images of nonprecipitating Sc overcasts photographed at USNA on (a) 30 August 2006 and (b) 12 January 2007. The mean image in (a) is calculated from 53 individual photographs and has a measured cloud base $z \sim 365\,\mathrm{m}$, whereas (b) is calculated from 78 photographs and has $2400\,\mathrm{m} < z < 2700\,\mathrm{m}$.

by breaks in the overcast in these directions, but so long as no clear sky is visible anywhere the cloud cover still satisfies my definition of overcast. At least at USNA, such horizon brightening is not rare in Sc overcasts, and it occurs over both land and the adjacent Chesapeake Bay.

Like Fig. 3, Fig. 5 also plots meridional curves of overcast chromaticities that are averaged temporally and azimuthally. Note that although both Figs. 3 and 5 are scaled isotropically in u' and v', Fig. 5 spans a much smaller colorimetric area ($\Delta u' = \Delta v' = 0.015$ in Fig. 5 as opposed to 0.025 in Fig. 3). Thus, while curvatures can be compared directly in these figures, Table 1 shows that their normalized chromaticity gamuts $\hat{g}$ are distinctly different [20]. Table 1's conventional meteorological abbreviations "OVC" and "CLR" indicate overcast and clear, respectively.

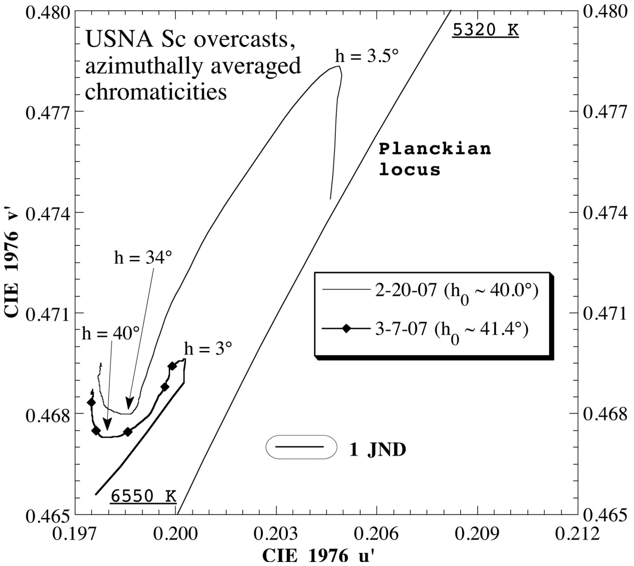

Fig. 5. Temporally and azimuthally averaged chromaticity curves for Sc overcasts measured at USNA on 20 February and 7 March 2007.

Differences in $\hat{g}$ aside, nearly every Sc overcast that we photographed has two distinct colorimetric turnings, one at high h and the other at low h. However, the turnings' details can vary considerably from day to day, just as they do in the clear sky. For example, Fig. 6 pairs an overcast with large, nearly symmetric turnings (9 November 2007 curve) with one where these features are vestigial (29 November 2006 curve). A few overcasts are bluest near the horizon, and this causes particularly large colorimetric excursions toward the blue at low h. The 30 August 2006 and 7 March 2007 Sc overcasts (Figs. 3 and 5, respectively) clearly show this fairly unusual behavior.

A simple semiempirical model suggests that this low-h turning toward the blue (i.e., toward higher color temperatures; see Section 4) is caused by bluish airlight whose radiances steadily increase with decreasing h until just above the horizon [21]. Perhaps surprisingly, overcasts thus repeat the clear sky's pattern of skylight reddening at intermediate h, followed by airlight bluing at lower h. Figure 7 illustrates this colorimetric behavior common to clear and overcast skies, although here the turning's direction at high h does differ for the two sky states (i.e., clockwise with decreasing h in the clear sky and counterclockwise in the overcast). Such subtle trends would be difficult indeed to observe without the detailed data provided by all-sky digital imaging.

B. Histograms of Chromaticity and Inverse Color Temperature

We can see even more colorimetric detail in overcasts by plotting two-dimensional histograms of their chromaticities. Although this added detail can be

Table 1. Mean Skylight Chromaticities and Chromaticity Gamuts

Figure	Date	Sky State	h_0 Interval^b (°)	Mean u'	Mean v'	$\hat{g}$
3	8-30-06	OVC	46.4–52.1	0.19883	0.47008	0.0034196
3^a	1-12-07	OVC	27.6–29.1	0.20037	0.47379	0.02275
5	2-20-07	OVC	40.1–39.9	0.1995	0.47063	0.012948
5^a	3-7-07	OVC	39.6–43.2	0.19865	0.46834	0.0042835
6	11-29-06	OVC	25.2–27.5	0.19954	0.47145	0.0053575
6	11-9-07	OVC	15.6–10.1	0.1964	0.4636	0.0068814
7	1-17-07	CLR	29.8	0.1783	0.42476	0.065473
7	10-5-06	OVC	15.2–9.4	0.19641	0.4665	0.0073714
8^a	1-12-07	OVC	27.6–29.1	0.19883	0.4706	0.014246
9^a	3-7-07	OVC	39.6–43.2	0.1986	0.46806	0.0058461
11	9-14-07	OVC	53.0–50.6	0.19905	0.47053	0.0069569

[a] For a given overcast, gamut $\hat{g}$ and mean u', v' depend slightly on whether chromaticities are first averaged azimuthally (Figs. 3 and 5) or not (Figs. 8 and 9).

[b] Morning observations list the smaller h_0 value first, whereas afternoon observations list it last.

instructive, it comes at the price of obscuring the angular distributions of overcast colors. For example, Fig. 8 is a histogram of all colors in the 12 January 2007 overcast (i.e., sans azimuthal averaging; compare Fig. 3), and its gray-scale legend scales relative frequency f_{rel} logarithmically. Thus the bright pixels clustered near $u' = 0.198$, $v' = 0.469$ indicate the predominance of those colors in this overcast. However, equally evident is Fig. 8's curve of low-f_{rel} pixels that arcs away from the Planckian locus and ends in Fig. 4(b)'s small but distinct band of yellowish overcast near the horizon.

Figure 8 provides information not found in Fig. 3, such as the fact that overcast chromaticities can be on the purplish or right-hand side of the Planckian locus. Not surprisingly, Fig. 8's individual chromaticities span a larger area on the CIE diagram than do their azimuthally averaged kin in Fig. 3. Neither figure likely jibes with our visual impression of Fig. 4(b)—isolated bands of yellow near the horizon appear to be paired with near monochromes elsewhere. Yet Figs. 3 and 8 together make clear that even this seeming dichotomy of color is in fact a continuum.

As Table 1 indicates, Fig. 8's overcast chromaticity gamut $\hat{g}$ is unusually large. More typical is Fig. 9's modest array of chromaticities for the much more uniform Sc overcast of 7 March 2007, for which $\hat{g}$ is only ~40% of its value on 12 January 2007. This reduced $\hat{g}$ stems from the absence in Fig. 9 of Fig. 8's near-horizon yellowing, which is itself caused by small areas of thinner overcast in Fig. 4(b). Even though $\hat{g}$ is much smaller in Fig. 9, the accompanying JND scale indicates that differences are still discernible among its overcast colors.

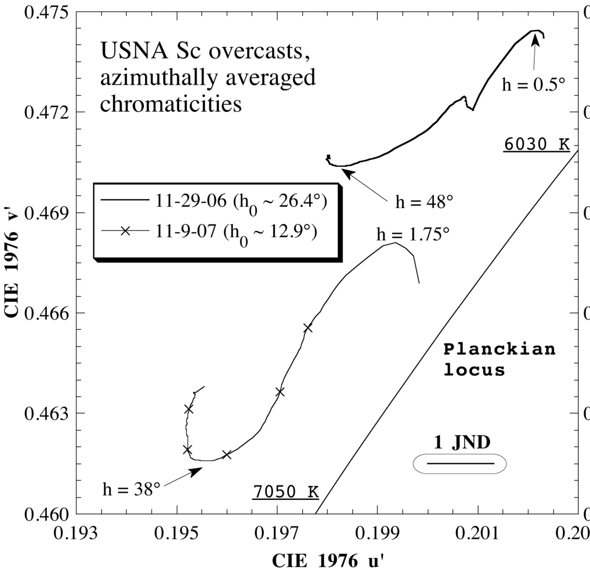

Fig. 6. Temporally and azimuthally averaged chromaticity curves for Sc overcasts measured at USNA on 29 November 2006 and 9 November 2007. Light drizzle fell throughout measurements on the latter date. To show more detail, the u', v' scaling is slightly anisotropic here.

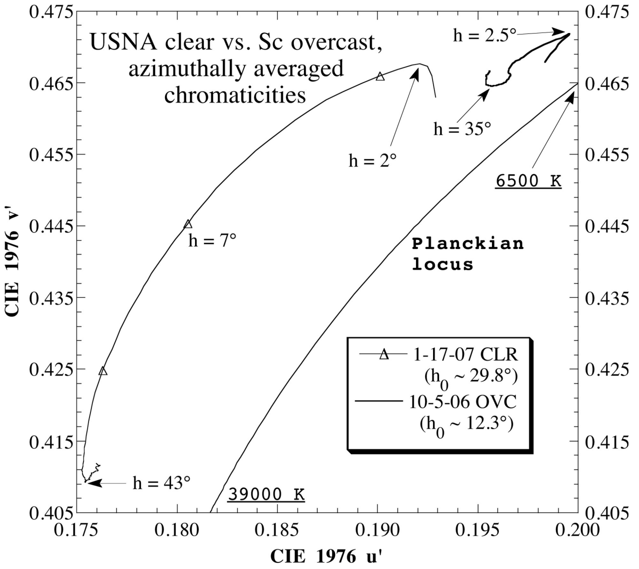

Fig. 7. Temporally and azimuthally averaged chromaticity curves for a clear (CLR) sky and a Sc overcast (OVC) measured at USNA on 17 January 2007 and 5 October 2006, respectively. The CLR chromaticities are averaged within two 90° wide sectors that are symmetric about the clear-sky principal plane (relative azimuths of 45°–135° and 225°–315°), so these colors exclude the solar and antisolar regions. To show as much detail as possible, the u', v' scaling is anisotropic here.

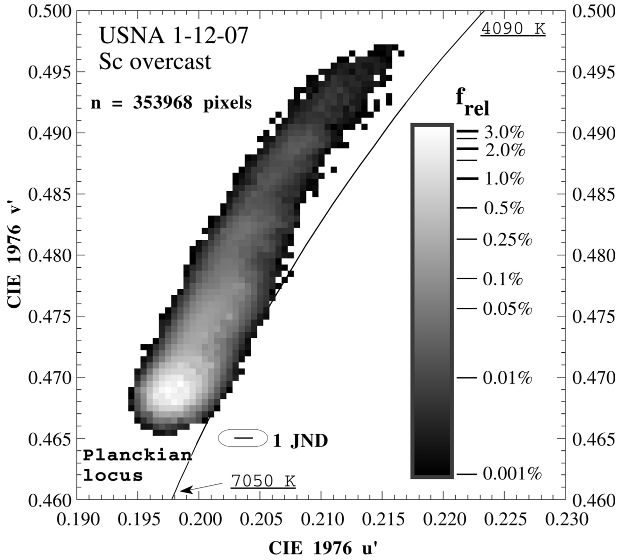

Fig. 8. Histogram of u', v' chromaticities for Sc overcast measured at USNA on the morning of 12 January 2007 when $27.6° < h_0 < 29.1°$. The absolute pixel frequency in any u', v' bin is the product of its gray-scale relative frequency f_{rel} and the total number of image pixels n.

Fig. 10. Time-averaged fisheye image calculated from 61 individual photographs of a Sc overcast photographed at USNA on 14 September 2007; the measured cloud base is ~2400 m. For consistency in printing, no image processing is used to correct the small, but constant, color bias of this and other RAW-format images (Figs. 4(a) and 4(b)).

Note that the modal colors in Figs. 8 and 9 occur near the blue ends of their chromaticity clusters, meaning that outlier (i.e., low-frequency) chromaticities in their overcasts tend to be yellower rather than bluer. However, Figs. 10 and 11 show that the reverse can be true: in the 14 September 2007 overcast, outlier chromaticities are bluer rather than yellower, as indicated by Fig. 11's swath of bright pixels to the left of its modal chromaticities at $u' = 0.199$, $v' = 0.471$. These outlier chromaticities occur mostly in Fig. 10's first trigonometric quadrant just above its horizon. Other bluish areas in Fig. 10 include the thin arcs that stretch across the sky and are slightly darker than their surroundings. As is true in Fig. 4(b), the simplest explanation for these long-lived arcs is persistent maxima in cloud τ along the mean flow. This increased cloud τ both decreases the arcs' radiances and increases their color temperatures (i.e., makes them slightly bluer) [6].

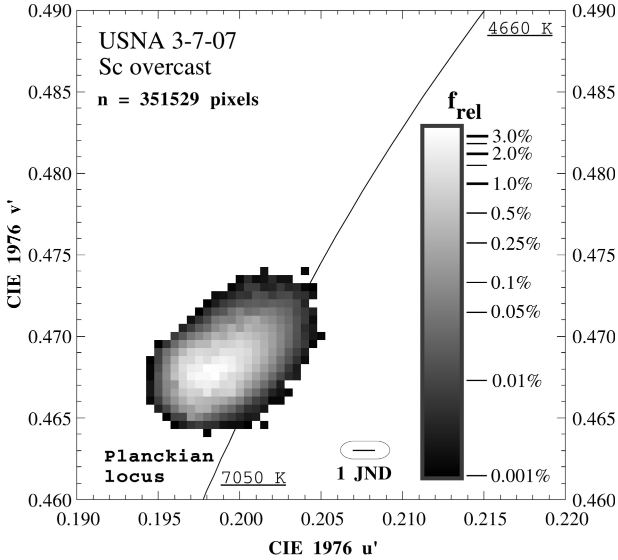

Fig. 9. Histogram of u', v' chromaticities for Sc overcast measured at USNA on the morning of 7 March 2007 when $39.6° < h_0 < 43.2°$. Throughout measurements, precipitation varied from light snow to flurries.

Correlated color temperature (CCT) has long served as an approximate, convenient alternative to chromaticity coordinates near the Planckian locus

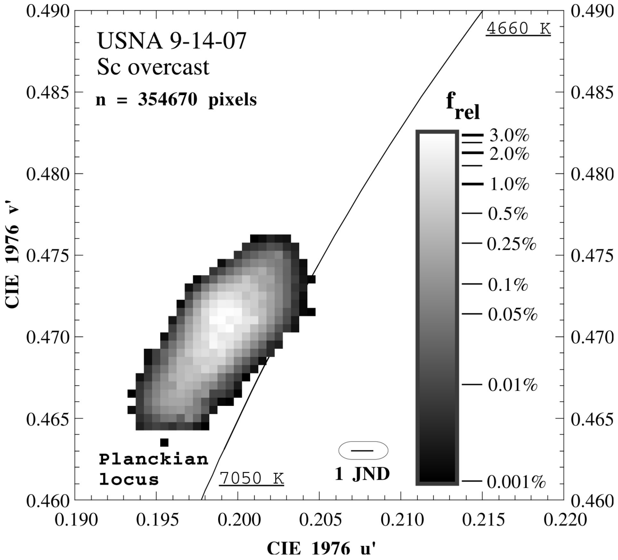

Fig. 11. Histogram of u', v' chromaticities for nonprecipitating Sc overcast measured at USNA on the afternoon of 14 September 2007 when $53.0° > h_0 > 50.6°$.

[22]. Because CCT reduces two-dimensional u', v' data to one dimension, CCT necessarily introduces some colorimetric ambiguity into quantifying overcast color [23]. For example, an overcast feature whose $\mathrm{CCT} = 6000\,\mathrm{K}$ can lie on either side of the Planckian locus. But since the perceptual consequences of this uncertainty often are moot for overcast colors, CCTs are useful here provided that we keep their limitations in mind. Even more useful than CCT itself is inverse CCT, which yields a scale that describes human color response more uniformly [5]. The unit of inverse CCT is the reciprocal mega-Kelvin (10^6/CCT), which is denoted by the symbol MK^{-1} and was originally called the “mired” [24].

Figure 12 interleaves histograms of inverse CCT for the 7 March 2007 and 14 September 2007 Sc overcasts; note that the ordinate is $\log_{10}(n)$, where n is the number of pixels in each inverse-CCT interval. On comparing Fig. 12’s inverse-CCT histograms with the corresponding chromaticity histograms in Figs. 9 and 11, notice how the bluer colors (i.e., those with smaller inverse CCTs) occur with greater relative frequency on 14 September 2007 than they do on 7 March 2007. In other words, the 14 September 2007 histogram in Fig. 12 is more symmetric about its modal color than is the 7 March 2007 histogram. Both the bluish horizon and faint arcs in Fig. 10 contribute to this enhanced blueness.

In Fig. 13, the abscissa scale changes in order to interleave the 7 March 2007 and 12 January 2007 histograms, a comparison that clearly reveals the latter overcast’s marked color skewness. Figure 13’s long tail of overcast colors with lower CCTs (and thus higher inverse CCTs) on 12 January 2007 is just as prominent and easy to quantify here as it is in Fig. 8.

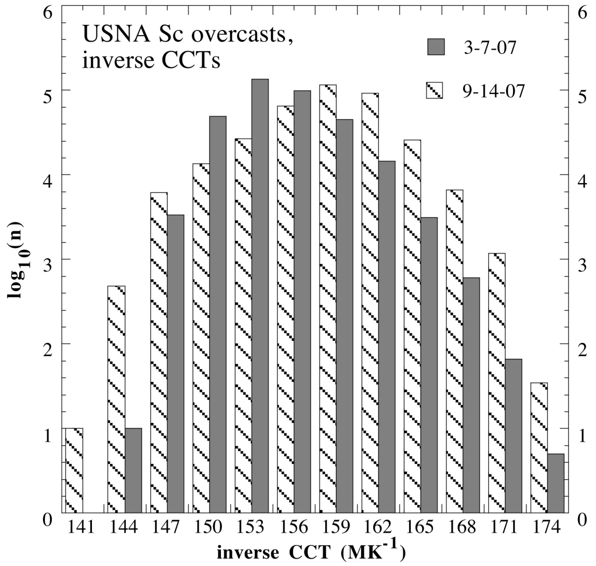

Fig. 12. Histograms of inverse CCT for overcasts measured at USNA on 7 March 2007 (solid bars) and 14 September 2007 (striped bars). Each bar’s height is proportional to $\log_{10}(n)$, where n is the number of pixels in the corresponding interval of inverse CCT. Each juxtaposed pair of bars for the two dates has a common abscissa value (e.g., the leftmost pair is for $144\,\mathrm{MK}^{-1}$).

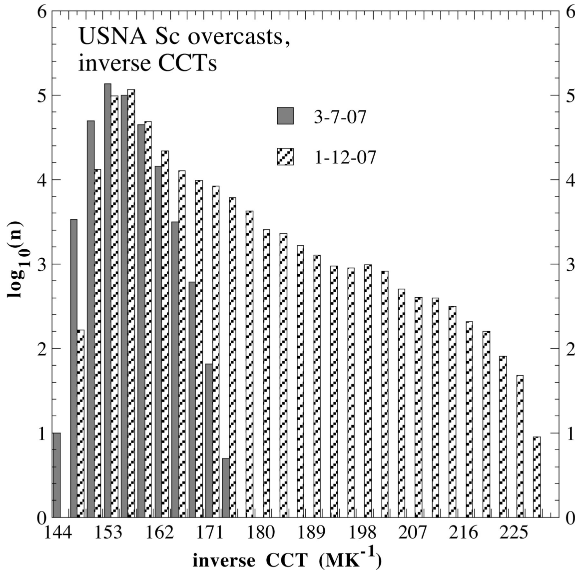

Fig. 13. Histograms of inverse CCT for overcasts measured at USNA on 7 March 2007 (solid bars) and 12 January 2007 (striped bars).

Once again, though, graphical clarity should not be confused with easy visibility: the continuum of colors present in Fig. 4(b) remains as difficult to quickly discern there as it is immediately obvious in Figs. 8 and 13. Yet one’s real-time experience of a constantly changing Sc overcast need not be divorced from such colorimetric order. Indeed, my experience is that foreknowledge makes such visual subtleties easier to see.

4. Modeling the Angular Distribution of Overcast Colors

Our past experience with general-purpose radiative transfer models such as MODTRAN4 suggests that they can simulate individual spectra of overcast radiances fairly realistically. This qualified endorsement means that, for a reasonable choice of input parameters, MODTRAN4 produces spectra that are nearly congruent with individual measured overcast spectra [6]. However, neither MODTRAN4 nor its predecessor LOWTRAN7 appears to simulate the angular *patterns* of overcast spectra and chromaticities particularly well.

Consider the divergence between these models and reality in Fig. 14. For the sake of comparison, Fig. 14 repeats Fig. 5’s meridional curve of the azimuthally averaged colors that were measured in the 20 February 2007 Sc overcast. Paired with these observations are comparable overcast chromaticity curves from LOWTRAN and MODTRAN. Each simulation uses its default Sc cloud model, with cloud bases set to either $z = 0.66\,\mathrm{km}$ or $z = 1.0\,\mathrm{km}$ above the surface and cloud thicknesses $\Delta z = 1.34\,\mathrm{km}$ or $\Delta z = 1.9\,\mathrm{km}$ (LOWTRAN and MODTRAN parameters, respectively). For each model, $h_0 = 45°$, and the viewing azimuth is 90° from the sun. Using only a single relative azimuth is acceptable because changing this

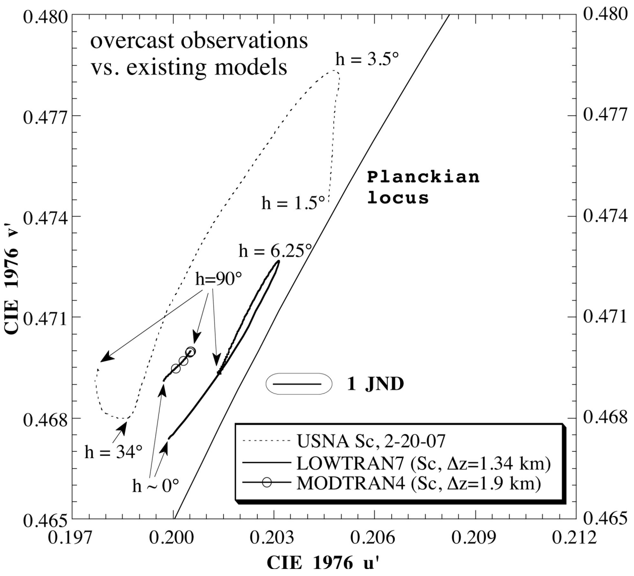

Fig. 14. Temporally and azimuthally averaged chromaticity curve for the 20 February 2007 Sc overcast compared with Sc simulations by LOWTRAN7 and MODTRAN4. For a wide range of input parameters, neither model predicts overcast chromaticity patterns well and both greatly underestimate typical overcast color gamuts.

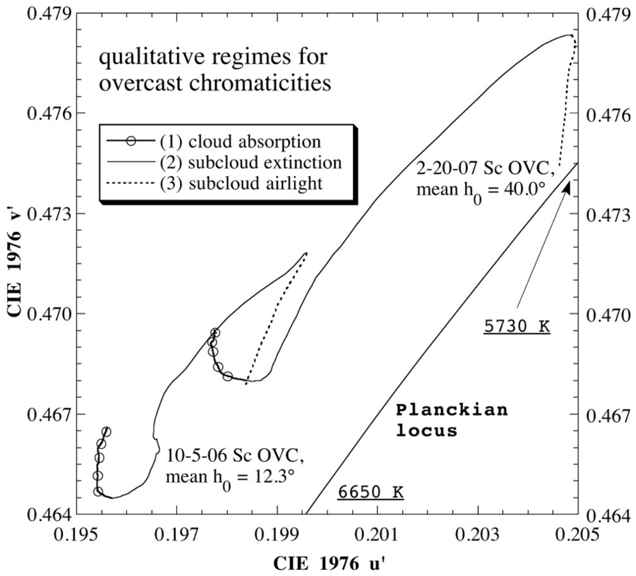

Fig. 15. Overcast chromaticity regimes typical of many overcasts and the changing balance of radiative transfer factors that explains them: (1) bluing caused by increasing spectral absorption in clouds from the zenith to $h \sim 30°$–$40°$, (2) reddening caused by increasing extinction beneath the overcast over ever-longer slant optical paths for $30°$–$40° > h > 3°$, and (3) bluing caused by increasing airlight for $h < 3°$.

parameter affects the models' chromaticities negligibly for such optically thick overcasts.

These models' overcast chromaticity patterns are odd indeed. Although all the overcasts that we measured exhibit just the *opposite* color trend, LOWTRAN predicts consistent reddening of the overcast from the zenith down to $h \sim 6°$, and only there does bluing begin. No more satisfactory is MODTRAN's claim that the Sc overcast becomes progressively bluer from the zenith until $h \sim 0.5°$, with a minuscule move toward the red thereafter. At such low h, MODTRAN's assumption of a plane-parallel atmosphere is problematic at best and may well contribute to its nonphysical behavior. Note too that MODTRAN's overcast color gamut is much smaller than either those predicted by LOWTRAN or observed outdoors. Changing overcast z and Δz does not affect the shape of either model's chromaticity curves much, which suggests that their verisimilitude problems cannot be solved simply by adjusting these parameters. Given the complexity of these models, the causes of their colorimetric problems are not immediately obvious.

Recall that observed overcast color patterns typically consist of (a) bluing from the zenith down to $h \sim 30°$–$40°$, followed by (b) reddening down to $h \sim 3°$, and finally (c) bluing down to the horizon. Figure 15 illustrates these three distinct color regimes as seen in overcasts photographed at markedly different h_0 on 5 October 2006 and 20 February 2007. A simple, physically plausible explanation for these regimes is that surface-based observers see a shifting balance between the spectral effects of (1) absorption within the overcast and both (2) extinction losses and (3) airlight gains that arise from scattering in the cloud-free air beneath it. Process (1) causes the initial bluing from the zenith to $h \sim 30°$–$40°$, while the latter two yield (2) reddening until a few degrees above horizon and then (3) bluing at still lower h.

My semiempirical model attempts to describe overcast colors realistically by combining spectrally selective absorption and scattering in the overcast and subcloud layers. Its theoretical basis is the radiative transfer equation [25], here given as

$$L_f = \underbrace{L_0 \exp(-\tau_f)}_{\mathbf{A}} + \underbrace{\int_0^{\tau_f} (J(\tau)\exp(\tau - \tau_f))\mathrm{d}\tau}_{\mathbf{B}}, \qquad (3)$$

where the radiance L_f received by an observer depends on the combined effects of terms **A** and **B**. Term **A** is the attenuated radiance L_0 for a distant light source (here the cloud base; see Fig. 16), and term **B** is an airlight term that represents the cumulative scattering effects of differential atmospheric volumes dV along any slant path from $\tau = 0$ at L_0 to τ_f, the total optical depth along the path between observer and cloud base. A source function $J(\tau)$ describes the scattering-angle dependence of dV's illumination by skylight radiances and the net radiance that dV scatters toward the observer. All terms in Eq. (3) are implicit functions of wavelength λ.

At visible λ below the cloud base, term **A** tallies source radiances *not* lost due to extinction by scattering along τ_f, while term **B** tallies gains of scattered radiance from the intervening air. Few real atmospheric $J(\tau)$ yield airlight integrals (term **B**) that can be

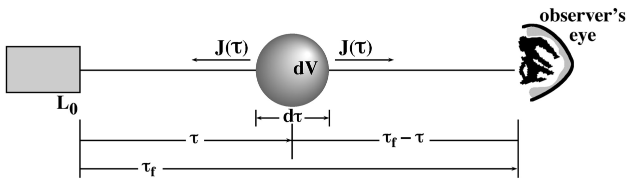

Fig. 16. Scattering geometry for an object of radiance L_0 seen by an observer through a multiple-scattering medium along a path of total optical depth τ_f. The path consists of differential air volumes dV, each having an angular scattering phase function $J(\tau)$. Here L_0 is the spectral radiance emerging from the cloud base and τ_f is for the nominally clear air beneath it.

evaluated analytically. But in the shallow air layer beneath many overcasts, we can reasonably assume that the $J(\tau)$ spectrum does not change significantly along a given slant path. In that case, the spectral radiative transfer equation reduces to $L_{f,\lambda} = L_{0,\lambda} \exp(-\tau_{f,\lambda}) + J_\lambda(1 - \exp(-\tau_{f,\lambda}))$.

The overcast model's empirical bases are measured values of (1) the cloud spectral transmissivities T_λ that yield L_0 [6], (2) the subcloud spectral extinction coefficients $\beta_{\text{ext},\lambda}$, with $\tau_f = \beta_{\text{ext}} s$ and $s =$ the slant-path geometrical distance to the cloud base, and (3) the subcloud J_λ spectrum, which varies with h but not along s at a given h.

What insights does this model yield? Figure 17 shows that, like the measured spectra, it produces three distinct chromaticity regimes. For the purposes of this initial demonstration, the model's chromaticity *trends* are more important than its absolute chromaticities: subsequent refinements in its empirical parameters will make the observed and simulated curves more nearly congruent. In regime (a), from the zenith to $h \sim 30°–40°$, the model overcast becomes progressively bluer with decreasing h because here the cloud absorption spectrum dominates and increases the bluish bias of L_0. This L_0 trend holds at all elevation angles because geometrical and optical slant paths through the overcast steadily increase as h decreases. But only in regime (a) does spectrally selective absorption by cloud droplets govern the overcast's color as seen from the surface.

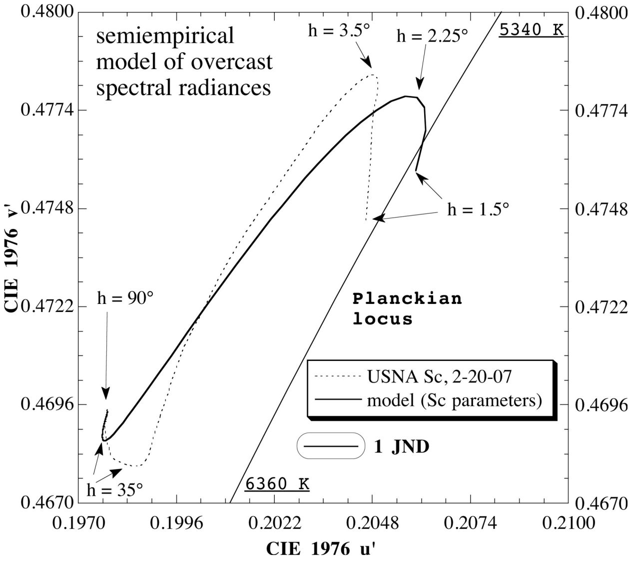

Fig. 17. Temporally and azimuthally averaged chromaticity curve for the 20 February 2007 Sc overcast compared with a simulation from the semiempirical model. Like MODTRAN and LOWTRAN, this model is based on the radiative transfer equation and, unlike them, it correctly reproduces the chromaticity gamuts and turnings observed in real overcasts.

In regime (b), for $30°–40° > h > 3°$, net reddening occurs because here the subcloud extinction spectrum [the $\exp(-\tau_f)$ factor in Eq. (3)'s term **A**] dominates. This is analogous to the progressive yellowing with distance of cumulus clouds on a clear day [1,2,26], especially when the sun is low in the sky: as subcloud τ_f increases with decreasing h, we can begin to see the consequences of clear-air scattering preferentially removing shorter wavelengths from the unscattered L_0 reaching us. Finally, progressive bluing occurs for $h < 3°$ in regime (c): at these largest subcloud τ_f, ever-increasing multiple scattering results in the predominance of bluish airlight [Eq. (3)'s term **B**]. Taken together, the model's absorption and scattering regimes yield a perhaps unexpected result: overcast and clear skies have as many radiative transfer similarities as they do differences.

5. Conclusions

These research results address two long-standing problems in the optics of overcast skies: capturing their surfeit of angular and temporal details while trying to divine some order from their seeming chaos. Our earlier time-series analyses of overcast color [6] and brightness [17] stressed overcasts' temporal patterns, while here the emphasis is on their time-averaged angular distributions of color. Naturally the chromaticity gamuts and details of these colors change perceptibly from one overcast to the next. Yet their underlying meridional structure is a remarkably consistent set of three distinct chromaticity regimes: (a) bluing from the zenith down to $h \sim 30°–40°$, then (b) reddening down to $h \sim 3°$, and finally (c) bluing down to the horizon. Furthermore, the colorimetric turnings that separate these overcast regimes are nearly always the same: for decreasing h, the first turning is counterclockwise and the second is clockwise. Although clear skies exhibit the same kind of turnings (Fig. 7), the one at higher h often is opposite its overcast counterpart.

Unlike existing models, the semiempirical model presented above helps explain this and other overcast color features. In both overcast and clear skies, the colorimetric turnings near the horizon seem to result from a shift between the predominance of reddish extinction at higher h and bluish airlight at lower h. In all such color regimes, scattering by cloud-free air determines what we see. Yet the high-h turnings differ for the two sky states because only in the overcast do we see a transition from the effects of cloud absorption to those of clear-air scattering. Such connections between the optics of clear and overcast skies appear obvious in hindsight, but they would be difficult indeed to make without the new, detailed views of overcasts made possible by all-sky imaging.

This research was generously supported by United States National Science Foundation grant ATM-0540896 and by the United States Naval Academy's Departments of Oceanography, Physics, and Mathematics. Opinions, findings, and conclusions or recommendations expressed in this paper are those of the author and do not necessarily reflect the views of the National Science Foundation.

References

1. M. Minnaert, *Light and Color in the Outdoors*, translated and revised by L. Seymour (Springer-Verlag, 1993), p. 325. This edition's foreword indicates that the book was first published in 1937, so Minnaert's earliest research predates the mid-1930s.
2. W. E. K. Middleton, *Vision through the Atmosphere* (U. Toronto Press, 1952), pp. 155–172.
3. A pioneering work on irradiance-based overcast color is W. E. K. Middleton's "The color of the overcast sky," J. Opt. Soc. Am. **44**, 793–798 (1954).
4. S. Nann and C. Riordan, "Solar spectral irradiance under clear and cloudy skies: measurements and a semiempirical model," J. Appl. Meteorol. **30**, 447–462 (1991).
5. J. Hernández-Andrés, R. L. Lee, Jr., J. Romero, and J. L. Nieves, "Color and spectral analysis of daylight in southern Europe," J. Opt. Soc. Am. A **18**, 1325–1335 (2001).
6. R. L. Lee, Jr. and J. Hernández-Andrés, "Colors of the daytime overcast sky," Appl. Opt. **44**, 5712–5722 (2005).
7. One early example is L. T. Maloney and B. A. Wandell, "Color constancy: a method for recovering surface spectral reflectance," J. Opt. Soc. Am. A **3**, 29–33 (1986).
8. R. L. Lee, Jr., "Colorimetric calibration of a video digitizing system: algorithm and applications," Color Res. Appl. **13**, 180–186 (1988).
9. D. Connah, S. Westland, and M. G. A. Thomson, "Recovering spectral information using digital camera systems," Coloration Technol. **117**, 309–312 (2001).
10. J. L. Nieves, E. M. Valero, S. M. C. Nascimento, J. Hernández-Andrés, and J. Romero, "Multispectral synthesis of daylight using a commercial digital CCD camera," Appl. Opt. **44**, 5696–5703 (2005).
11. PR-650 spectroradiometer from Photo Research, Inc., 9731 Topanga Canyon Place, Chatsworth, Calif. 91311. According to Photo Research, at specified radiance levels a properly calibrated PR-650 measures luminance and radiance accurate to within ±4%, has a spectral accuracy of ±2 nm, and its CIE 1931 colorimetric errors are $x < 0.001$, $y < 0.001$ for a 2856 K blackbody (CIE standard illuminant A).
12. J. Romero, A. García-Beltrán, and J. Hernández-Andrés, "Linear bases for representation of natural and artificial illuminants," J. Opt. Soc. Am. A **14**, 1007–1014 (1997).
13. J. Hernández-Andrés, J. L. Nieves, E. M. Valero, and J. Romero, "Spectral-daylight recovery by use of only a few sensors," J. Opt. Soc. Am. A **21**, 13–23 (2004).
14. For any pair of chromaticities separated by $\Delta u'$ and $\Delta v'$, calculate this error as the Euclidean distance $\Delta u'v' = [(\Delta u')^2 + (\Delta v')^2]^{1/2}$.
15. G. Wyszecki and W. S. Stiles, *Color Science: Concepts and Methods, Quantitative Data and Formulae*, 2nd ed. (Wiley, 1982), pp. 306–310.
16. All photographs are corrected for the effective integrated transmissivity of this fisheye lens as a function of angle from its optical axis, but tests show that no additional spectral corrections are needed to the transform matrix **F**.
17. R. L. Lee, Jr. and J. Hernández-Andrés, "Short-term variability of overcast brightness," Appl. Opt. **44**, 5704–5711 (2005).
18. For example, see *Spatial Distribution of Daylight—CIE Standard Overcast Sky and Clear Sky*, CIE Standard S 003/E-1996 (Commission Internationale de l'Eclairage, 1996), p. 3.
19. R. L. Lee, Jr. and D. E. Devan, "Observed brightness distributions in overcast skies," Appl. Opt. **47**, H116–H127 (2008).
20. For a definition of $\hat{g}$, see R. L. Lee, Jr., "Twilight and daytime colors of the clear sky," Appl. Opt. **33**, 4629–4638, 4959 (1994).
21. R. L. Lee, Jr., "Horizon brightness revisited: measurements and a model of clear-sky radiances," Appl. Opt. **33**, 4620–4628, 4959 (1994).
22. D. B. Judd, D. L. MacAdam, and G. Wyszecki, "Spectral distribution of typical daylight as a function of correlated color temperature," J. Opt. Soc. Am. **54**, 1031–1040 (1964).
23. J. Hernández-Andrés, R. L. Lee, Jr., and J. Romero, "Calculating correlated color temperatures across the entire gamut of daylight and skylight chromaticities," Appl. Opt. **38**, 5703–5709 (1999).
24. [15], pp. 224–225.
25. C. F. Bohren and E. E. Clothiaux, *Fundamentals of Atmospheric Radiation* (Wiley-VCH, 2006), p. 294.
26. C. F. Bohren, *Clouds in a Glass of Beer: Simple Experiments in Atmospheric Physics* (Wiley, 1987), p. 149.